catalysts

MDPI

Article

Platinum-Modified Mixed Metal Oxide Electrodes for Efficient Chloralkaline-Based Energy Storage

Jamylle Y. C. Ribeiro [1,2,3], Gessica O. S. Santos [3,4], Aline R. Dória [1,4], Iñaki Requena [3], Marcos R. V. Lanza [4], Katlin I. B. Eguiluz [1,2], Giancarlo R. Salazar-Banda [1,2], Justo Lobato [3,*] and Manuel A. Rodrigo [3,*]

1 Electrochemistry and Nanotechnology Laboratory, Institute of Technology and Research (ITP), Aracaju 49032-490, SE, Brazil; jamyllerib@gmail.com (J.Y.C.R.); alinerdoria@gmail.com (A.R.D.); katlinbarrios@gmail.com (K.I.B.E.); gianrsb@gmail.com (G.R.S.-B.)
2 Graduate Program in Processes Engineering (PEP), Tiradentes University, Aracaju 49032-490, SE, Brazil
3 Chemical Engineering Department, Faculty of Chemical Sciences and Technologies, Universidad Castilla-La Mancha, 13004 Ciudad Real, Spain; gessicasantiago@usp.br (G.O.S.S.); inaki.requena@uclm.es (I.R.)
4 São Carlos Institute of Chemistry, University of São Paulo, São Carlos 13566-590, SP, Brazil; marcoslanza@usp.br
* Correspondence: justo.lobato@uclm.es (J.L.); manuel.rodrigo@uclm.es (M.A.R.)

Abstract: In this work, a series of novel mixed metal oxide (MMO) electrodes with the composition $Ti/RuO_2Sb_2O_4Pt_x$ ($0 \leq x \leq 10.0$) were developed, envisaging their application in a reversible electrochemical cell based on the chloralkaline process as an energy storage system. These electrodes were synthesized via the ionic liquid method. Comprehensive physical, chemical, and electrochemical characterizations were conducted to evaluate their performance. The feasibility of employing these electrodes within reversible processes was explored, using the products generated during the electrolytic operation of the system for fuel cell operation. During the electrolyzer operation, higher current densities resulted in enhanced current efficiencies for the production of oxidized chlorine species. Notably, the presence of platinum in the catalyst exhibited a negligible impact on the coulombic efficiency at low current densities where water oxidation predominates. However, at higher current densities, the presence of platinum significantly improved coulombic efficiency, approaching values of approximately 60%. Transitioning to a fuel cell operation, despite the improved kinetic performance associated with a higher platinum content, the process efficiency was predominantly governed by ohmic losses. Curiously, the MMO electrode made without platinum ($Ti/(RuO_2)_{70}$-$(Sb_2O_4)_{30}$) displayed the lowest ohmic losses. This study establishes optimal conditions for future investigations into this promising possibility, which holds great potential for energy storage via chloralkaline-based reversible reactions.

Keywords: reversible electrochemical cells; mixed metal oxide; platinum; efficiency; hydrogen; energy storage

Citation: Ribeiro, J.Y.C.; Santos, G.O.S.; Dória, A.R.; Requena, I.; Lanza, M.R.V.; Eguiluz, K.I.B.; Salazar-Banda, G.R.; Lobato, J.; Rodrigo, M.A. Platinum-Modified Mixed Metal Oxide Electrodes for Efficient Chloralkaline-Based Energy Storage. *Catalysts* **2024**, *14*, 152. https://doi.org/10.3390/catal14020152

Academic Editor: Bruno Fabre

Received: 18 December 2023
Revised: 19 January 2024
Accepted: 5 February 2024
Published: 18 February 2024

1. Introduction

Within the context of the increasing necessity of energy and the threat of global warming, renewable energies are becoming one of the most important bets of modern society [1,2] for trying to maintain our actual level of life [3]. The main drawback of these more sustainable sources of energy is finding the proper way to fit the production and demand of energy. In order to solve this drawback, energy storage is becoming a real bottleneck because, after decades of development, there is not a clear and efficient solution yet. In this context, hydrogen (H_2) is a universal fuel considered an interesting and promising alternative for this storage of renewable energy [4–7], and its production and consumption using electrochemical technology can be reached with almost zero carbon emissions, which meets the so-called carbon neutralization goal [8] and is very important to fight against global warming. Although nowadays there are mature technologies for

its production and use, with electrolyzer and fuel cell technologies developed at the technology readiness level (TRL) 9, there is still a gap and necessity for the development of new technologies. One of the applications for H_2 generation is the brine electrolysis process, which produces chlorine, hydrogen gases, and caustic soda. This process has been used in the chloralkaline industry for decades [4,9–11] for manufacturing chlorine and caustic soda as commodities. However, little attention was focused on the use of the produced hydrogen until recently, in which many efforts have been devoted to improving the energy efficiency of chloralkaline electrolysis [8] and the production of electricity from chlorine (Cl_2) and H_2 produced in the system.

The use of mixed metal oxide (MMO) electrode formulations and the special cell design are directly related to the performance and efficiency of the process for generating H_2-Cl_2 [12]. According to the literature, one of the oxides that are advantageous for use in the composition of MMOs is ruthenium oxide (RuO_2) due to its high efficiency in its behavior in the chlorine evolution reactions (oxidation and reduction) and also because it shows great stability for the chlorine release reaction [13,14]. However, it undergoes strong corrosion in acidic media. An alternative to optimizing this problem is to add antimony, as it is a promising structural component with high electrical conductivity and thermodynamic stability at low pH. Additionally, to optimize the electrolysis performance, Pt has a highlight for increasing the kinetics of the H_2 redox reaction in reversible cells. In other studies, such behavior was confirmed [15,16].

So far, there is no published work using MMO electrodes with the compositions of Sb, Pt, and Ru mixed oxides for reversible cell applications. These anodes can be applied in a reversible cell for H_2-Cl_2 generation. The operation of a reversible electrochemical cell is based on the operating modes of the fuel cell and the electrolyzer, which operate in the same electrochemical cell and the same electrodes. This type of cell has flexibility in operation that allows it to be operated in both modes, one to store surplus energy as hydrogen and the other to obtain electricity from the stored hydrogen when required.

With this background, the research hypothesis is that the novel MMO electrodes, consisting of various compositions of RuO_2, antimony, and platinum, could exhibit distinct performance in a novel liquid-liquid chloralkaline reversible cell set-up. Therefore, this study aims to investigate the effectiveness of these electrodes in both electrolysis and fuel cell modes, assessing their potential for chlorine and hydrogen production during electrolysis and the generation of electricity during fuel cell operation.

Depositing coatings of ruthenium and antimony oxides and platinum with different ratios of Ru, Sb, and Pt in their formulation onto titanium plates and using conventional heating in an electric furnace yields distinct electrode configurations ($Ti/(RuO_2)_{70}$-$(Sb_2O_4)_{30}$, $Ti/(RuO_2)_{66.5}$-$(Sb_2O_4)_{28.5}$-Pt_5, and $Ti/(RuO_2)_{63}$-$(Sb_2O_4)_{27}$-Pt_{10}). They were characterized physically, chemically, and electrochemically and were evaluated as anodes in electrolyzers and cathodes in fuel cells, driving the chloralkaline process in a reversible electrochemical cell configuration for an energy storage system.

2. Results

2.1. Physical and Electrochemical Characterization of Manufactured MMO Electrodes

In this investigation, three mixed metal oxide electrodes containing ruthenium and antimony oxides with different ratios of platinum were made following a thermal decomposition methodology for use in chloralkaline reversible cells. The SEM images observed in Figure 1A–C show the morphologies of the three resulting electrodes. All the electrodes have a coating with the appearance of "cracked mud", which is a typical morphology of oxide electrodes synthesized via thermal decomposition techniques [17,18]. Furthermore, it is possible to identify cracks on the surface of the electrodes that are attributed to mechanical stress arising from the plasticity of the coating and differences in the coefficients of thermal expansion between the substrate and the film formed during the calcination process [19,20]. Although the morphology remains similar, the inclusion of 5% platinum in the catalyst results in a surface with the presence of deeper cracks. Conversely, with 10% platinum, the

morphology undergoes a change, presenting as the most compact and recovered surface with the presence of shallow cracks. Initially, the morphology of oxide anodes is expected to influence the chlorine catalytic reaction significantly [21]. The presence of cracks and pores in the coatings introduces external and internal surfaces, which behave in a distinct manner. The external surface, directly exposed to the electrolyte, readily interacts with dissolved ions, thereby giving ease of accessibility.

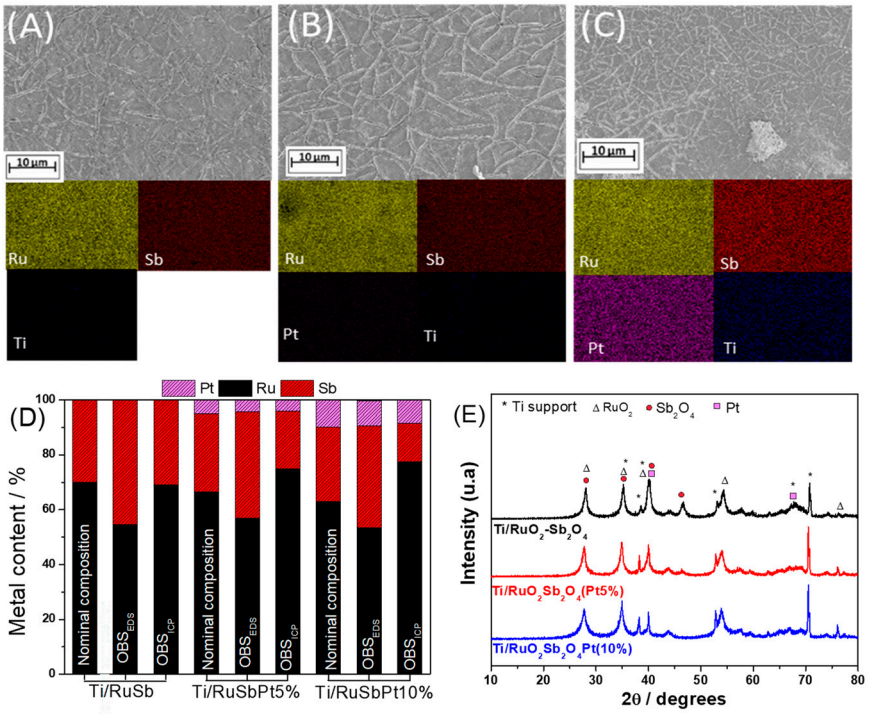

Figure 1. SEM images of (**A**) Ti/$(RuO_2)_{70}$-$(Sb_2O_4)_{30}$, (**B**) Ti/$(RuO_2)_{66.5}$-$(Sb_2O_4)_{28.5}$-Pt_5, and (**C**) Ti/$(RuO_2)_{63}$-$(Sb_2O_4)_{27}$-Pt_{10}. Left: images obtained with BS mode. Right: elemental mapping obtained in BSE mode. (**D**) Molar content according to analysis from ICP and EDS, and (**E**) XRD diffraction patterns of electrodes.

In contrast, the internal surface, which resides within the confines of cracks, grain boundaries, and pores, is less accessible to the electrolyte. Notably, the rapid kinetics of the chlorine evolution reaction make the external surface the main active phase. Additionally, under conditions of intense gas evolution, the internal surface might be blocked by adherent gas bubbles, leading to diminished activity in chlorine evolution [20]. The metal content for each electrode was measured by Inductively Coupled Plasma-Atomic Emission Spectrometry (ICP-AES). The obtained results (Figure 1D) show that anodes presented very close values among nominal and measured metal contents, as evidenced by the ICP analysis. The mapping images (Figure 1A–C) and energy-dispersive X-ray (EDX) spectroscopy analysis (Table S2) clearly reveal a uniform dispersion of all constituent metals across the electrode surface. This consistent distribution is further substantiated by the notable concordance between the theoretical composition and the experimentally determined values.

From the XRD analysis presented in Figure 1e, discernible crystalline phases are identified. The tetragonal structure of RuO_2 [22] Joint Committee on Powder Diffraction Standards (JCPDS 40-1290), Sb_2O_4 [23] (JCPDS 36-1163), and the face-centered cubic (FCC) metallic platinum phase (JCPDS 04–0802) [24,25] are unambiguously observed. Furthermore, it is evident that peaks associated with titanium are less intense for the electrode containing 10% platinum, which is in agreement with SEM images. In contrast, for the other two electrodes (5% platinum and no platinum), the Ti peak intensities are quite similar, consistent with SEM observations that revealed the presence of deeper cracks, leading to

higher absorption/diffraction of X-rays by the Ti substrate [26]. These results highlight the efficacy of the chosen methodology and the applied temperature in facilitating the formation of both metallic oxides and platinum.

2.2. Electrochemical Characterization of the Prepared Electrodes

In the electrochemical characterization of the three novel MMO electrodes investigated in this study, Figure 2 presents the performance characterization of an electrolyte containing sulfuric acid. Here, redox features are observed between 0.6 and 1.2 V vs. Ag/AgCl and are generally associated with the Ru^{3+}/Ru^{4+} redox pair. This phenomenon arises from the adsorption of water, wherein protons or hydroxide sites can penetrate into the porous electrode [27]. Notably, the voltammetric profiles underwent changes for the electrodes containing platinum, where reduction peaks observed within the 0.6 to 0.4 V vs. Ag/AgCl region can be attributed to the oxygen reduction (PtO reduction), which is characteristic of platinum electrodes. This observation confirms the presence of platinum-active sites on the electrode surface. On the other hand, the electrochemical behavior significantly varies when we change from electrolytes comprising sulfate as anions to those containing chlorides, as shown in Figure 3. The cyclic voltammetry measurements conducted with a 2 mol L^{-1} NaCl electrolyte show a rapid increase in current density around 1.1 V vs. Ag/AgCl, corresponding to the chlorine evolution reaction (CER). This event, involving the oxidation of Cl^- to Cl_2, overlaps with the region of OER. Consequently, competition between CER and OER is expected during bulk electrolysis. Within the potential range from 1.3 to 0.9 V vs. Ag/AgCl, a reduction peak emerges ascribed to the reduction of Cl_2 back to Cl^- [28]. Nyquist plots reveal the high conductivity of all three anodes with respect to Cl_2 formation (applied potential of 1.14 V vs. Ag/AgCl for all anodes). The inset within Figure 3 illustrates that the curves are almost superimposed, which means that activity toward CER is expected to be similar for these anodes.

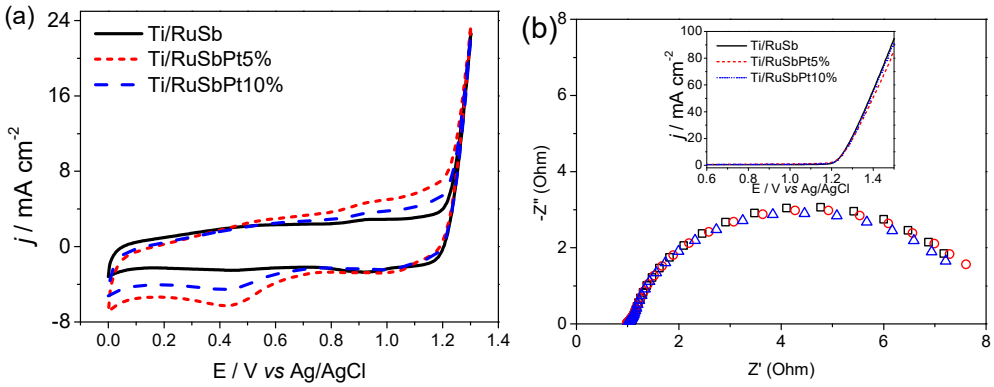

Figure 2. (**a**) Cyclic voltammograms. (**b**) Nyquist plots obtained using $Ti/(RuO_2)_{70}$-$(Sb_2O_4)_{30}$, $Ti/(RuO_2)_{66.5}$-$(Sb_2O_4)_{28.5}$-$Pt_{0.5}$, and $Ti/(RuO_2)_{63}$-$(Sb_2O_4)_{27}$-Pt_{10} electrodes. Electrolyte: H_2SO_4 0.5 mol L^{-1}. Scan rate: 50 mV s^{-1}. T = 25 °C. Inset: linear sweep voltammetry curves.

Another crucial parameter for the in-situ characterization of MMO electrodes is the morphology factor analysis. Given the coating irregularities in rough/porous electrodes, different contributions from internal and external active sites are anticipated. Thus, following the methodology outlined by Da Silva et al. [19], consecutive voltammetric curves were recorded at various scan rates, covering a narrow capacitive potential interval (here from 0.55 to 0.75 V). A plot of capacitive current versus scan rate (Figure 4) was generated. In this plot, the first linear region at a lower scan rate is associated with the total capacitance ($C_T = C_I + C_E$), representing the sum of internal and external capacitances, while the second linear segment at higher scan rates is linked to the external capacitance. The morphology factor is calculated as the ratio of internal and total capacitance ($\varphi = C_T - C_I$), with values ranging between 0 and 1. This parameter describes the fraction of the film's topography that is more challenging to assess.

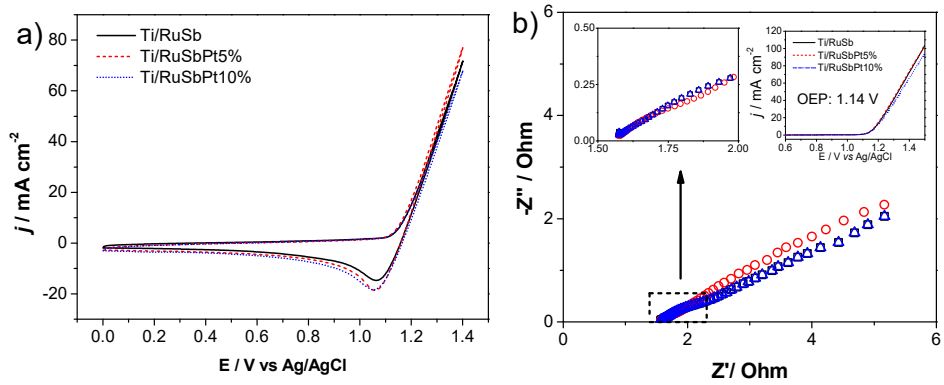

Figure 3. (**a**) Cyclic voltammograms and (**b**) Nyquist plots obtained for Ti/$(RuO_2)_{70}$-$(Sb_2O_4)_{30}$, Ti/$(RuO_2)_{66.5}$-$(Sb_2O4)_{28.5}$-$Pt_{0.5}$, and Ti/$(RuO_2)_{63}$-$(Sb_2O_4)_{27}$-Pt_{10} electrodes. Electrolyte: 2 mol L^{-1} NaCl solution; scan rate: 50 mV s^{-1}. T = 25 °C. Inset: linear sweep voltammetry curves.

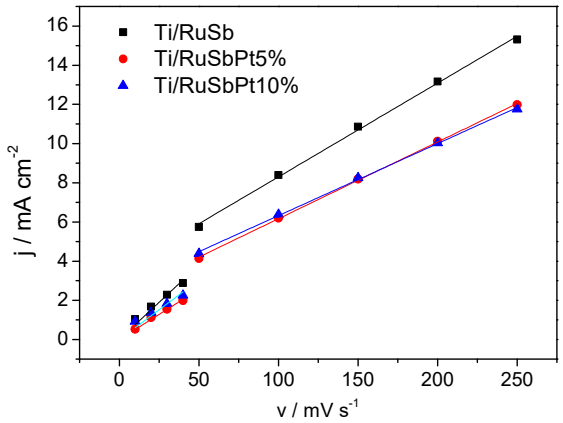

Figure 4. Plot depicting the dependence of capacitive current (j) on scan rate for Ti/$(RuO_2)_{70}$-$(Sb_2O_4)_{30}$, Ti/$(RuO_2)_{66.5}$-$(Sb_2O_4)_{28.5}$-$Pt_{0.5}$, and Ti/$(RuO_2)_{63}$-$(Sb_2O_4)_{27}$-Pt_{10} electrodes.

The capacitances (C_T, C_E, and C_I) and morphology factor values ($\varphi = C_I/C_T$) obtained for the different electrodes are depicted in Table 1. As a general trend, it is noteworthy that morphology factors approximate 0, indicating a small contribution of internal sites in the electrodes produced here. These data suggest that despite differences in surface morphologies, the contributions of external and internal sites are similar. Furthermore, both electrodes with platinum exhibit lower capacitances, potentially associated with more compact surfaces.

Table 1. Total, external, and internal capacitances (C_T, C_E, and C_I) and morphology factor for the different electrodes.

Electrode	C_T/mF cm^{-2}	C_E/mF cm^{-2}	C_I/mF cm^{-2}	φ
Ti/$(RuO_2)_{70}$-$(Sb_2O_4)_{30}$	76	48	28	0.37
Ti/$(RuO_2)_{66.5}$-$(Sb_2O_4)_{28.5}$-Pt_5	51.3	39	12	0.24
Ti/$(RuO_2)_{63}$-$(Sb_2O_4)_{27}$-Pt_{10}.	60.8	37	24	0.39

2.3. Performance of the Chloralkaline Electrolyzer

This work goes beyond the state of the art, and novel electrodes were evaluated in a single reversible chloralkaline-based electrochemical cell as an energy storage system. To achieve this, the electrode with a Ti/$(RuO_2)_{66.5}$-$(Sb_2O_4)_{28.5}$-$Pt_{0.5}$ composition was evaluated as a reference to understand the general behavior of the proposed system as it had an intermediate amount of platinum in relation to the MMO electrodes evaluated in this work.

The evaluation of electrode performance within reversible electrochemical cells began in electrolysis mode. This preliminary step included galvanostatic electrolysis conducted under both soft (50 mA cm^{-2}) and harsh (150 mA cm^{-2}) conditions. These conditions of current densities were selected after the evaluation of the voltammetric characterization, with the aim of evaluating a region near the beginning of the competition of the CER and OER (soft conditions) and another region closer to a realistic operational regime of an electrolyzer (harsh conditions) characterized by negligible mass transport limitations. It is important to state that during the tests, no significant changes in the cell voltage were observed, indicating that the electrodes did not undergo any relevant change during the harsh electrolytic conditions applied during electrolysis, therefore highlighting the stability of the electrodes in short-term applications. As illustrated in Figure 5, alterations in the pH and corresponding cell voltage values were outlined during the electrolysis of a 2.0 mol L^{-1} NaCl solution within an electrochemical cell equipped with an electrode with 5% Pt, denoted as Ti/$(RuO_2)_{66.5}$-$(Sb_2O_4)_{28.5}$-Pt_5, at two different current densities: 50 and 150 mA cm^{-2}.

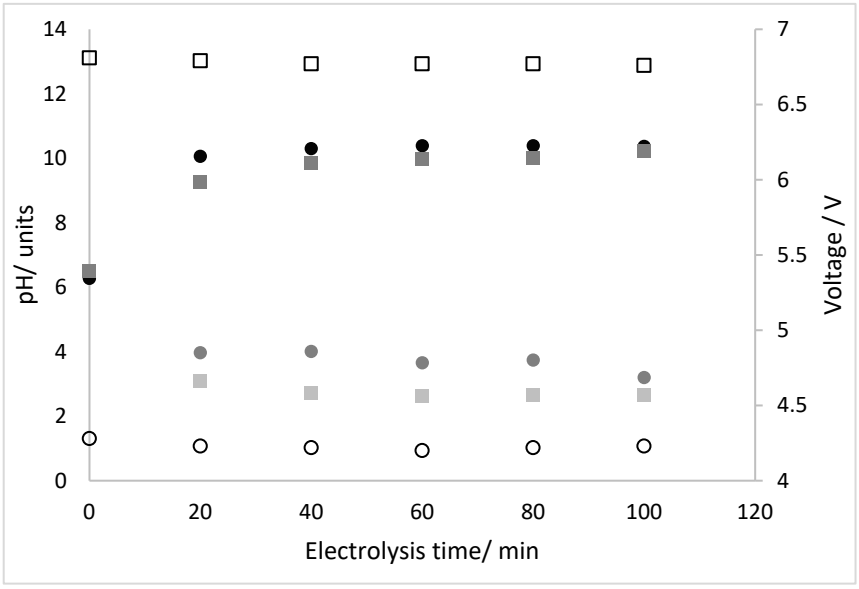

Figure 5. Changes in the pH ((●) pH catholyte, 50 mA cm^{-2}; (■) pH catholyte, 150 mA cm^{-2}; (●) pH anolyte, 50 mA cm^{-2}; (■) pH anolyte, 150 mA cm^{-2}; primary axis) and cell voltage ((○) voltage at 50 mA cm^{-2}, and (□) voltage at 150 mA cm^{-2}; secondary axis) during the electrolysis of 2.0 mol L^{-1} sodium chloride aqueous solutions.

It is evident that substantial alterations in the pH occurred within both the anolyte and catholyte during both electrolysis tests. The deviations were more pronounced in the anolyte, in which the decrease was 0.53 units higher when a current density of 150 mA cm^{-2} was applied (2.67 as compared to the test in which the current density applied was 50 mA cm^{-2} with a value of 3.20). Initially, the increase in Pt within the catholyte can be associated with the reduction of water to hydrogen, as represented by Equation (1). Conversely, the decrease observed in the anode is more intricate as the set of reactions that occur in this compartment is more complex, but it may be primarily attributed to the oxidation of water to oxygen, as denoted by Equation (2). The greater change in pH observed under higher current densities can be attributed to a larger generation of protons [29]. The preservation of a constant cell voltage throughout the tests implies the absence of surface alterations during the process.

$$2H_2O + 2e^- \rightarrow H_2 + 2OH^-, \quad (1)$$

$$2H_2O \rightarrow O_2 + 4H^+ + 4e^-, \quad (2)$$

Figure 6 shows the production of oxidized chlorine species (OCS) during the operation of the cell. After 100 min of electrolysis, the quantity of OCS produced when the electrochemical cell was in electrolysis mode amounted to 32.84 and 188.26 mg in the respective tests. Differences in these values can be attributed to the considerable variation in the electric charge passed within the same period: 0.086 and 0.247 Ah for 50 and 150 mA cm^{-2}, respectively.

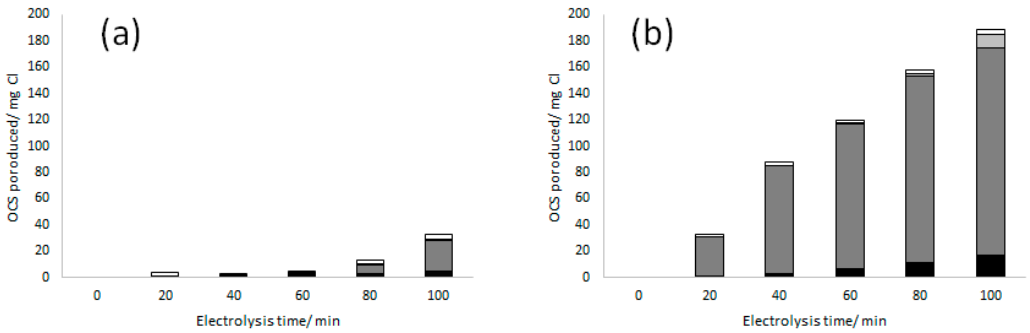

Figure 6. Distribution of OCS produced during the electrolysis carried out at 50 mA cm^{-2} (**a**) and 150 mA cm^{-2} (**b**) in the different sections of the electrochemical cell. Anode gas: black; anode liquid: dark gray; cathode gas: light gray; cathode liquid: white.

Chlorine is generated by the direct oxidation of chloride anions on the anode surface (Equation (3)). Chlorine can be released either as a gas (Equation (4)) or undergo disproportionation into hypochlorous acid following Equation (5). The deprotonation of hypochlorous acid, which is a weak acid, to yield hypochlorite is promoted within neutral to alkaline pH ranges [30] because the pKa of this reaction is 7.53 (Equation (6)). Additionally, the conversion of hypochlorous acid into its corresponding anhydride is also feasible (Equation (7)). Most of these reactions are reversible, and consequently, the grouping of all these oxidized chlorine species into the OCS category makes sense. This group is rationalized by the limitations intrinsic to characterization techniques, which could potentially modify the speciation.

$$2Cl^- \rightarrow Cl_2(aq) + 2e^-, \quad (3)$$

$$Cl_2(aq) \leftrightarrow Cl_2(g), \quad (4)$$

$$Cl_2(aq) + H_2O \leftrightarrow ClO^- + Cl^- + 2H^+, \quad (5)$$

$$HClO \leftrightarrow ClO^- + H^+, \quad (6)$$

$$2HClO \leftrightarrow Cl_2O + H_2O, \quad (7)$$

Nevertheless, considering the pH range of the anolyte (2.5−4.0) and the well-known dependence of the speciation of oxidized chlorine on the pH, a mixture consisting primarily of HClO and Cl_2(aq) is expected in the anolyte. Likewise, the stripping of Cl_2(g) by the oxygen generated through the OER could significantly impact the speciation of the system, resulting in a pronounced shift in the reaction shown in Equation (2) and the consequent production of mixed O_2/Cl_2 gas.

However, an unexpected observation was that OCS were measured in significant amounts in both liquid and gas phases in the anodic and cathodic compartments, indicating a substantial penetration of chlorine species through the membrane from the anode to the cathode. This observation persisted despite the employment of a new membrane in all tests, and no visible damage or degradation was evident from a visual point of view.

The proportion of oxidized chlorine crossing over to the cathode exhibited a greater effect in the case of operation at lower current densities, reaching a value as high as 19.27 ± 6.46% of the total OCS produced, which is 7.5 times higher than the corresponding value observed in tests conducted at elevated current densities (2.56 ± 0.32%); how-

ever, these figures can lead to a wrong interpretation of results because the amounts of OCS crossing from the anolyte to the catholyte (in terms of mg rather than a percentage) are quite similar. This observation stresses that the crossover rate is primarily limited by the inherent membrane characteristics and not governed by the operational current density. The differences in percentages are associated with the total production levels. Consequently, the values are substantially diminished in scenarios involving operations at higher current densities. Thus, values of the crossover calculated from mass balance were 0.0198 ± 0.0107 mg min^{-1} cm^{-2} in in the test made at 50 mA cm^{-2} and 0.0234 ± 0.009 mg $min^{-1}cm^{-2}$ in the test made at 150 mA cm^{-2}. The slight differences in these values can be rationalized regarding the notably elevated concentration generated in the anode at 150 mA cm^{-2} (almost six-fold greater). This high difference in concentration between the anolyte and catholyte causes a more pronounced concentration gradient, effectively amplifying the driving force for crossover.

Evidently, the phenomenon of OCS crossover through membranes constitutes a notable vulnerability within chloralkaline technology [31]. Given the implications for both electrolyzer and fuel cell applications, important efforts should be made in the forthcoming years to address this challenge for the development of robust and efficient reversible cells.

Significant differences are likewise evident between the production yields reached at the two current densities applied, thereby pointing out that oxygen evolution was favored at softer operation conditions with this specific electrode. Figure 7 shows the alterations in both coulombic efficiency and energy input to the cell throughout the duration of the tests. In the context of OCS production, the coulombic efficiency averages at 14.98 ± 8.76% in the test carried out at 50 mA cm^{-2}, which is more than four times lower than the corresponding outcome reached in the test performed at a high current density (59.18 ± 5.85%); however, the higher voltage required for this harsher condition results in a higher energy consumption, as also displayed on the secondary axes of the graph. This elevated energy demand results in a concomitant reduction in energy efficiency, albeit the magnitude of the decrease is lower when operating at 50 mA cm^{-2}. Specifically, the energy efficiency stands at 45.32 ± 27.49 mg $(Wh)^{-1}$ for 50 mA cm^{-2}, and comparatively, it is 2.5 times lower than the corresponding value at 150 mA cm^{-2}, which is 113.56 ± 11.48 mg $(Wh)^{-1}$.

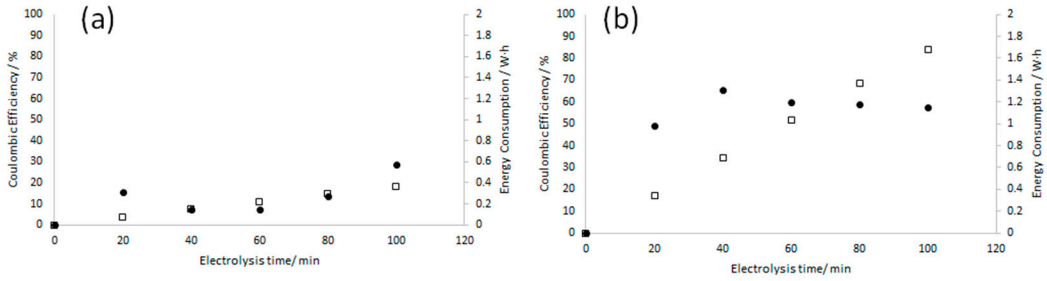

Figure 7. Changes in the coulombic efficiency (●) and energy powered (□) during the electrolysis of 2.0 mol L^{-1} sodium chloride aqueous solutions at 50 mA cm^{-2} (**a**) and 150 mA cm^{-2} (**b**).

Concerning the partitioning of OCS between the gaseous and liquid phases, it is evident that there was a negligible disparity in the ratios quantified within the catholyte for both tests. Specifically, the percentage of OCS present in the gas phase was 29.91% (50 mA cm^{-2}) and 31.16% (150 mA cm^{-2}) of the total content within this compartment. At first, this information may appear contradictory to the pH range observed in the catholyte. Under the pH conditions reached in both tests on the cathode side (over 10 units), a considerable proportion of OCS should exist in the form of hypochlorite anions according to the pKa of the $HClO/ClO^-$ system. Hence, the production of gaseous chlorine is not expected. This observation indicates that the observed crossover through the membrane is primarily associated with the transport of chlorine gas rather than dissolved molecular hypochlorous acid.

More pronounced discrepancies emerge concerning the distribution between the gas and liquid phases within the anolyte. Although the pH is more acidic when operating at 150 mA cm^{-2}, the ratio of gaseous chlorine was much higher at 50 mA cm^{-2}, constituting 50.78% of the total oxidized chlorine in a gaseous form. This proportion strongly contrasts with the corresponding value of 6.07% reached at 150 mA cm^{-2}. This dissimilarity can be explained by considering the enhanced efficiency of oxygen production and the concurrent stripping effect facilitated by this oxygen. This stripping phenomenon accelerates the transference of chlorine from the liquid to the gas phase at a lower current density. Notwithstanding, differences between relative and absolute values should be considered and remain pivotal. Notably, the absolute quantities of chlorine gas produced are obviously higher when operating at higher current densities due to the greater chlorine production, despite volatilization being less critical in percentage.

Hydrogen production was determined through two methodologies: by quantifying the amount collected in the gasometers and by a simulation based on the observed pH changes in both the anode and cathode. As seen in Figure 8, the outcomes from both approaches were very similar, which means that the set of reactions proposed is similar to the experimental behavior. Notably, in both tests, the experimental values were below the expected value according to a faradaic efficiency of 100%. These values are depicted, respectively, by the discontinuous and continuous lines corresponding to 50 and 150 mA cm^{-2}. This discrepancy indicates that the reduction of water competes with the reduction of chlorine in the cathodic compartment. This discrepancy, derived from the absence of reactions occurring consistently on other side, i.e., on the cathode surface—hydrogen peroxide formation, for instance—is improbable due to the low oxygen concentration being limited by solubility and transport limitations through the membrane.

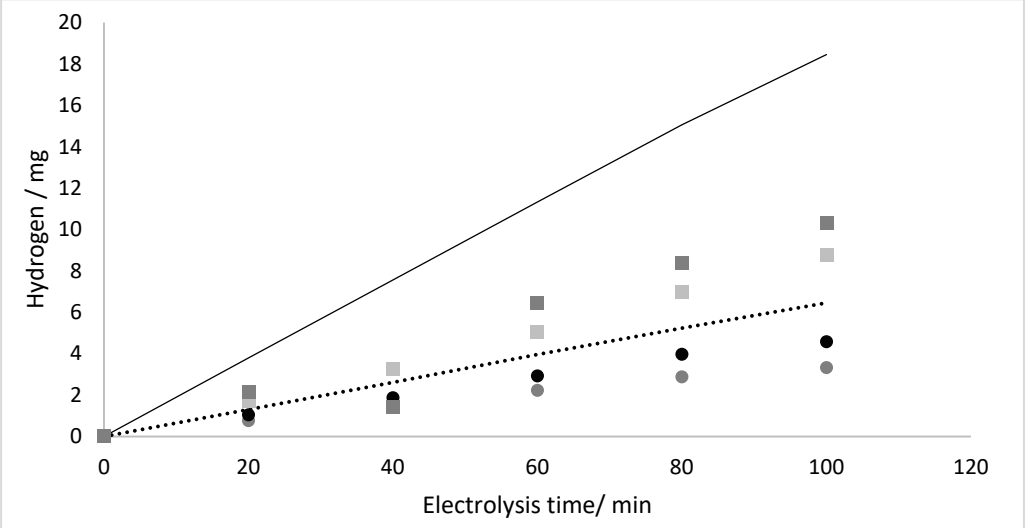

Figure 8. Evolution of hydrogen over time at two different current densities, 50 mA cm^{-2} and 150 mA cm^{-2}, during the electrolysis of 2.0 mol L^{-1} sodium chloride aqueous solutions ((•) hydrogen in gasometer at 50 mA cm^{-2}, (■) hydrogen in gasometer at 150 mA cm^{-2}, (•) hydrogen obtained from the mass balance between protons and hydroxyls at 50 mA cm^{-2}, and (■) hydrogen obtained from the mass balance between protons and hydroxyls at 150 mA cm^{-2}). Continuous and dashed lines correspond with the theoretical value, assuming a 100% efficiency obtained at 150 mA cm^{-2} and 50 mA cm^{-2}, respectively.

2.4. Performance of the Chloralkaline Fuel Cell

Because of relatively easy chlorine redox kinetics, H_2/Cl_2 fuel cells can operate with little activation loss associated with the chlorine electrode, in contrast to the H_2/O_2 fuel cells [32,33]. Thus, following the operation of the system equipped with the Ti/$(RuO_2)_{66.5}$-$(Sb_2O_4)_{28.5}$-Pt_5 electrolyzer configuration, the device was reconfigured as a fuel cell to

power a miniature engine. This phase involved a two-hour operation employing the hydrogen and chlorine stored in the gasometers. This reversal in the polarity of the cell transforms the anode into the cathode of the reversible electrochemical cell. The dynamics during this interval, including the intensity, power output, chlorine consumption, and pH fluctuations within the chlorine compartment are shown in Figure 9. The reversible operation mode demonstrated good progress, characterized by the sustained generation of electricity. Substantial hydrogen and oxidized chlorine species (OCS) consumption was noted, thus leading to a decreased pH in the catholyte. This pH decline implies the transformation of chlorine into chloride, an outcome driven by the migration of protons to preserve the balance of ionic charges within the system.

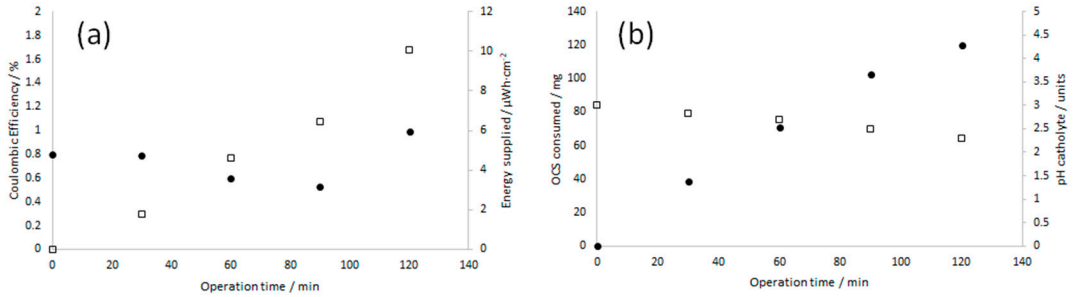

Figure 9. Changes in the different indicators during the operation of the reversible cell equipped with the electrode as a fuel cell and fed with the hydrogen, and the OCS produced during the electrolysis tests at 150 mA cm^{-2}. (**a**) (●) Operation current density, (□) energy supplied to the engine, (**b**) (●) OCS consumed, and (□) pH in the catholyte.

These results demonstrate the viability of employing reversible electrochemical cells in the context of chloralkaline technology operating with MMO electrodes consisting of mixtures of Ru, Sb, and Pt. Importantly, the same reagents generated during the electrolyzer mode can be easily redirected to feed an electricity-consuming device, thus establishing the inherent dual functionality of this system.

2.5. Impact of Platinum Content in Electrocatalysts

The temporal evolution of key parameters shown for the test involving the Ti/$(RuO_2)_{66.5}$-$(Sb_2O_4)_{28.5}$-Pt_5 (5% platinum) electrode is quite close to those observed in tests carried out with the Ti/$(RuO_2)_{70}$-$(Sb_2O_4)_{30}$ (0% platinum) and Ti/$(RuO_2)_{63}$-$(Sb_2O_4)_{27}$-Pt_{10} (10% platinum) electrodes, both in electrolysis and fuel cell mode. Remarkably, no relevant differences are worth reporting with respect to their general behavior, which may be explained in terms of the consistent employment of the same experimental apparatus and process conditions.

In the context of electrolyzer operation, the only relevant information produced using the novel MMO electrodes with different compositions were the changes observed in the efficiencies in the production of OCS. These changes are shown in Figure 10, wherein the coulombic efficiencies are displayed versus the platinum content of the MMO used. The inclusion of platinum in the catalyst did not substantially impact the coulombic efficiency in low-current-density operations, wherein the OER is the primary process; however, at higher current densities, noticeable trends appear. It could be pointed out that the presence of platinum positively influenced efficiency, and it is particularly evident in the considerable mitigation of the side reaction that generates oxygen. This improved efficiency reached levels approaching 60% due to platinum's involvement.

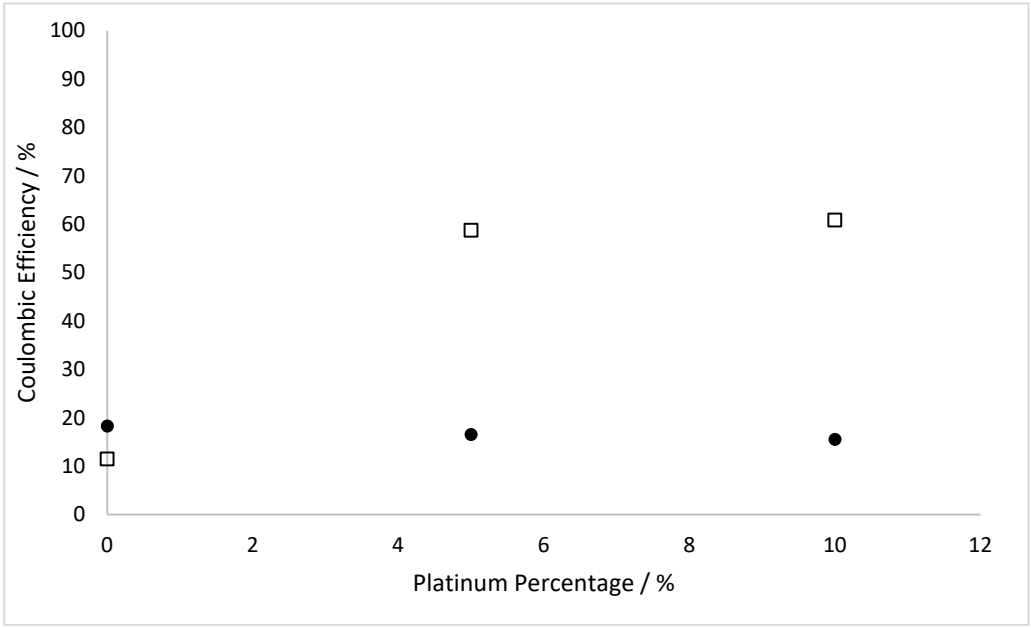

Figure 10. Influence of the platinum content of the mixed metal oxide electrodes on the average coulombic efficiency of the production of OCS during the electrolysis of 2.0 mol L^{-1} sodium chloride aqueous solutions at (●) 50 mA cm^{-2} and (□) 150 mA cm^{-2}.

Regarding the influence of the platinum content of the MMO electrode on the reversible mode operation (as a fuel cell), analogous results were observed in cells using the other two electrodes when compared to the Ti/$(RuO_2)_{66.5}$-$(Sb_2O_4)_{28.5}$-Pt_5. The average intensity exerted and applied voltage during the 2 h tests for each configuration are detailed in Table 2. Noteworthy distinctions in these metrics can be explained in terms of the interfacing/connection of the fuel cell with the compact device used to consume the energy.

Table 2. Average current intensity and cell voltage during the fuel cell tests performed to evaluate the effect of platinum.

Anode	Current Density (mA cm^{-2})	Voltage (mV)
Ti/$(RuO_2)_{70}$-$(Sb_2O_4)_{30}$	2.22	4.34
Ti/$(RuO_2)_{66.5}$-$(Sb_2O_4)_{28.5}$-Pt_5	0.742	6.68
Ti/$(RuO_2)_{63}$-$(Sb_2O_4)_{27}$-Pt_{10}	1.262	7.06

Hence, from the comparative analysis, it becomes pertinent to show the influence of the platinum content of the electrocatalyst on the polarization and power curves. This information is displayed in Figure 11, which unexpectedly indicates that the cell equipped with the anode without platinum operated better than the cells equipped with electrodes that have platinum in their composition. Moreover, the comparative evaluation of cells endowed with electrodes with 5% and 10% platinum content in their composition revealed negligible differences in operational efficacy. Although altering concentrations of Ru and Sb to include Pt (5 or 10%) led to a similar overall morphology and electrochemical performance, maybe the affinity of antimony to platinum, as reported by Jalalpoor et al. [34], can block the catalytic Pt sites, resulting in the lower overall performance of these anodes containing Pt.

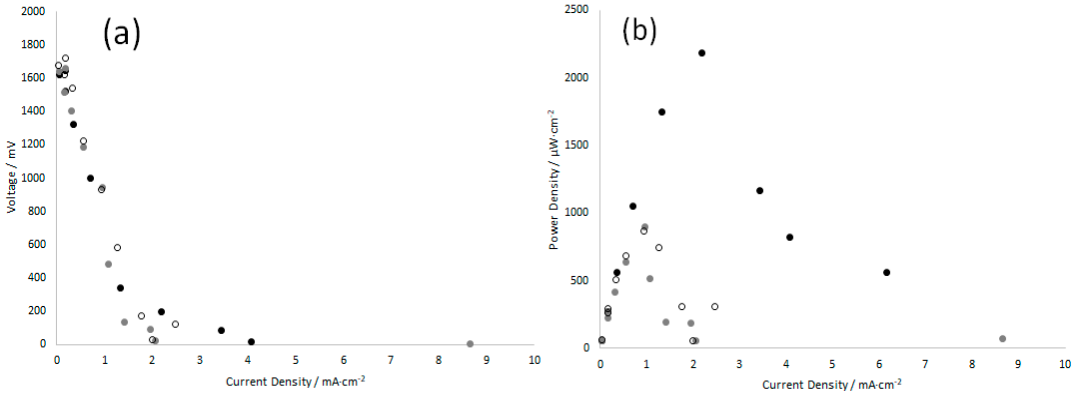

Figure 11. Polarization (**a**) and power (**b**) curves of the reversible electrochemical cell operated as a fuel cell with the cathode of (●) $Ti/(RuO_2)_{70}$-$(Sb_2O_4)_{30}$; (●) $Ti/(RuO_2)_{66.5}$-$(Sb_2O_4)_{28.5}$-Pt_5; (○) $Ti/(RuO_2)_{63}$-$(Sb_2O_4)_{27}$-Pt_{10}.

In a previous study, three different electrodes ($Ti/Ru_{0.5}Ir_{0.5}O_2$, $Ti/Ru_{0.3}Ti_{0.7}O_2$, and $Ti/Ru_{0.3}Ti_{0.6}O_2Pt_{0.1}$) were investigated for the oxidation of chlorides and reduction of chlorine in a reversible chloroalkaline cell, revealing a positive effect electrode containing platinum only in fuel cell mode [8]. Moreover, the power density achieved in the present study for the Pt-free MMO electrodes exceeds that obtained in the earlier research [15] using the Pt-free MMO based on Ti. It's noteworthy that the anode contained Pt in the previous work, whereas in the current study, the anode electrode is based on PbO_2. This means that the novel Pt-free MMO electrode assessed in this work emerges as a promising candidate for chloroalkaline-based reversible cells for energy storage. This is attributed to its ability to not only facilitate the oxidation of chlorine species (electrolysis mode) but also their reduction (fuel cell mode).

The composition of the electrocatalyst is crucial for achieving high catalytic activity and ensuring material durability in reversible energy devices. For instance, Deng et al. [24] investigated the core-shell structure of Zn-NC/GD made using a solvothermal method and high-temperature pyrolysis for potential application in efficient rechargeable Zn-air batteries (ZABs). Cyclic voltammetry was employed to analyze the oxygen reduction reaction (ORR) performance. Zn-NC/GD demonstrated excellent ORR performance, indicated by a high starting potential and high half-wave potential (Eonset = 0.95 V, E1/2 = 0.86 V), comparable to commercial Pt/C catalysts (Eonset = 1.01 V, E1/2 = 0.85 V). Additionally, Zn-NC/GD exhibited a smaller Tafel slope compared to Zn-NC, Zn-NC-W, and Pt/C, suggesting favorable ORR kinetics. These results prove that the structure of the electrocatalyst can efficiently improve ORR activity. Similarly, Deng et al. [25] investigated the utilization of Fe-pyridine N catalysts in rechargeable Zn-air batteries. The bifunctional Fe/Fe-NC-3 catalyst demonstrated superior ORR and OER electrochemical activity, closely approaching the performance of commercial Pt/C and IrO_2 catalysts with a rapid kinetic reaction (61.6 mV dec^{-1}). Notably, the catalyst exhibited remarkable stability over 500 h, high power density (304.4 mW cm^{-2}) in reversible ZABs, and flexibility in flat/bent states, providing a high open circuit voltage of 1.35 V and maintaining a stable voltage during discharge at 2 mA cm^{-2}. These studies present promising catalysts for potential applications in metal-air batteries.

3. Materials and Methods

3.1. Chemicals

All chemical reagents used were of analytical grade and were used without any additional purification. They are summarized as shown in Table S1. All solutions were prepared using ultrapure water obtained from a Gehaka Master All 2000 System (Sao Paulo, Brazil) (18.2 MΩ cm, 25 °C).

3.2. Preparation of MMO Anodes

The pre-treatment of the titanium plates was performed according to previous works [35], which consists of chemical attacks in HCl 20% (*w*/*w*) and oxalic acid 10% (*w*/*w*), respectively, for 15 min after boiling of each solution. After pre-treatment, titanium substrates were coated with previously prepared precursor solutions to obtain catalytic coatings with the following compositions: $(RuO_2)_{70}$-$(Sb_2O_4)_{30}$, Ti/$(RuO_2)_{66.5}$-$(Sb_2O_4)_{28.5}$-Pt_5, and Ti/$(RuO_2)_{63}$-$(Sb_2O_4)_{27}$-Pt_{10}. The precursor solutions were prepared using the 2-hydroxyethylammonium acetate (2HEAA) ionic liquid to dissolve the metallic precursors ($RuCl_3$, $SbCl_3$, and $H_2PtCl_6{\cdot}6H_2O$) [17]. Once prepared, the obtained ink was deposited on pre-treated titanium plates for subsequent calcination in a furnace at 350 °C for 5 min (heating rate 10 °C min^{-1}). The brushing and calcination steps were repeated until all the electrodes reached the same mass loading of 1.2 mg cm^{-2} of metal oxides (corresponding to a nominal thickness of around 2–3 µm). Final calcination for 60 min at 350 °C was finally carried out to eliminate any remaining organic matter.

3.3. Electrochemical Set-Up and Reversible Electrochemical Cell

A conventional Pyrex®glass (Mervilab, Madrid, Spain) three-electrode cell was used to carry out the electrochemical characterizations on a potentiostat/galvanostat (AUTOLAB–PGSTAT302N, Utrecht, The Netherlands). The prepared MMO anodes (geometric area = 2 cm^2) were used as the working electrode, a graphite bar as the counter electrode, and the reference electrode was a silver–silver chloride (Ag/AgCl, KCl 3.0 mol L^{-1}). Firstly, electrodes were characterized in 0.5 mol L^{-1} H_2SO_4 solution by means of cyclic voltammetry experiments (potential limits of 0–1.3 V vs. Ag/AgCl) at several scan rates (10–250 mV s^{-1}), where the morphology factor (a measure of electrochemical porosity) of oxide layers and other parameters as total, external, and internal capacitances were obtained according to the methodology proposed by da Silva et al. [36]. Linear sweep voltammetry (LSV) and electrochemical impedance spectroscopy (EIS) were also conducted in H_2SO_4 media, where oxygen evolution potential (OEP) values were determined for each anode as the potential where occurs the interception between the linear extrapolation of the rapid increase in current (which is related to OER) and the linear extrapolation of the baseline. Nyquist plots were obtained using Ti/$(RuO_2)_{70}$-$(Sb_2O_4)_{30}$, Ti/$(RuO_2)_{66.5}$-$(Sb_2O_4)_{28.5}$-$Pt_{0.5}$ and Ti/$(RuO_2)_{63}$-$(Sb_2O_4)_{27}$-Pt_{10} electrodes. Electrolyte: H_2SO_4 0.5 mol L^{-1}. scan rate: 50 mV s^{-1}. T = 25 °C. Inset: linear sweep voltammetry curves. The EIS measurements were carried out within the frequency range from 0.1 to 1000 Hz using an amplitude signal of 10 mV. After that, the same electrochemical measurements (CV, LSV, and EIS) were carried out using 2 mol L^{-1} NaCl solutions to understand the general behavior of anodes in this medium.

The reversible electrochemical reactor was composed of two compartments divided by a Nafion® 117 proton exchange membrane (Fuel Cell store, Bryan, TX, USA). In the anodic compartment, the three different MMO anodes with an exposed area of 1 cm^2 were evaluated, while in the cathodic compartment, a PbO_2-coated Ti electrode was used. For operation in the electrolysis mode, the two compartments of the cell were fed with concentrated NaCl solutions (2.0 mol L^{-1}), stored in the reservoir tanks, one for the anode and the other with the cathode, which were continuously recirculated using two peristaltic pumps. The Cl_2 was stored in the anode gasometer and the H_2 in the cathode gasometer, whereas the NaOH was collected in the reservoir tank of the cathode. The measurements of the accumulated volume were made using a millimeter ruler, and in fuel cell mode, the poles were reversed; that is, the accumulated hydrogen from the cathode gasometer started to be injected into the cell, producing electricity. A multimeter was used to measure the voltage values.

3.4. Chemical Analysis

During the experiments, samples were withdrawn from the anodic and cathodic compartments. The pH was measured using a GLP22 Crison pH meter (Hach, Barcelona,

Spain), and the conductivity was measured using a GLP31 Crison conductivity meter. Before use, the devices were periodically calibrated. To determine the chlorine that reacted, samples were collected in the anode and cathode compartments with a time interval of 20 min. A total of 3 mL of the samples in both compartments were collected to measure absorbance. In the liquid phase, 3 mL of the sample was used together with 50 µL of concentrated NaOH (3 mol L^{-1}), and in the gaseous phase, 5 mL of concentrated NaOH (3 mol L^{-1}) was used together with 5 mL of withdrawn gas. The absorbance of this sample is measured using an Agilent Cary Series 300 UV–Vis Spectrophotometer (Agilent, Santa Clara, CA, USA) at a wavelength of 293 nm. This methodology can also be found elsewhere [37].

3.5. Physical Characterization

The surface morphology of the anodes was seen using a field emission scanning electron microscope (FE-SEM) (Zeiss Gemini SEM 500, Zeiss, Oberkochen, Germany). The elemental chemical composition of the anodes was determined through energy-dispersive X-ray (EDX) spectroscopy coupled with scanning electron microscopy (EDX-SEM) equipment (Zeiss Gemini SEM 500, Zeiss, Oberkochen, Germany). Crystallographic phases present in the MMO anodes were identified by X-ray diffraction (XRD) on a Philips PW-1700 diffractometer (Philips, Amsterdam, The Netherlands) using CuKα radiation (λ = 1.5418 Å) at a scanning rate of 2° min^{-1} from 20° to 80°. The XRD patterns were analyzed using the X'pert High Score Plus software 3.0, and the data obtained were compared with the Joint Committee on Powder Diffraction Standards (JCPDS) database.

The elemental compositions of the samples were determined by Inductively Coupled Plasma-Atomic Emission Spectrometry (ICP-AES) using a Spectro spectrometer model Arcos (Miami, FL, USA). The detection limit (LD: 0.01 mg L^{-1}), and quantification limit (LQ: 0.10 mg L^{-1}).

4. Conclusions

From this work, the following conclusions can be drawn:

1. The manufacturing process of three MMO electrodes (Ti/$(RuO_2)_{70}$-$(Sb_2O_4)_{30}$, Ti/$(RuO_2)_{66.5}$-$(Sb_2O_4)_{28.5}$-Pt_5, and Ti/$(RuO_2)_{63}$-$(Sb_2O_4)_{27}$-Pt_{10} was successful and yielded a uniform distribution of metals across their surfaces. Furthermore, these electrodes demonstrated exceptional stability, as evidenced by their sustained performance without any signs of deterioration throughout both electrolyzer and fuel cell operational modes.
2. Mixed metal oxide (MMO) electrodes of Ti/$RuO_2Sb_2O_4Pt_x$ ($0 \leq x \leq 10.0$) can be satisfactorily produced via the ionic liquid method and applied in chloralkaline liquid–liquid reversible electrochemical cells. The same hydrogen and oxidized chlorine species that are generated during the electrolysis process can be efficiently employed as fuel in the subsequent operation as a fuel cell, leading to the generation of electricity and hence acting as an energy storage system.
3. The application of the developed anodes in electrolyzers for chlorine production revealed intriguing insights. At lower current densities (50 mA cm^{-2}), current efficiency values remain low (~20%) and are almost independent of the composition of the electrode. In contrast, at higher current densities (150 mA cm^{-2}), the influence of platinum in chlorine electrochemistry can be significantly observed. The inclusion of platinum has notably elevated the efficiencies towards chlorine formation, achieving an impressive increase of up to 60.5%.
4. In the fuel cell operational mode, the performance of the system is seriously limited by the ohmic losses. The electrode composition without platinum (Ti/$(RuO_2)_{70}$-$(Sb_2O_4)_{30}$) exhibits superior performance owing to its lower resistance. Nonetheless, the inclusion of platinum content in the electrocatalyst enhances kinetic performance, as indicated by polarization curves.

Supplementary Materials: The following supporting information can be downloaded at https://www.mdpi.com/article/10.3390/catal14020152/s1. Table S1: Main chemicals used in this work. Table S2: Determination of the nominal and experimental proportion of metals in the oxide films.

Author Contributions: Author Contributions: Conceptualization, J.Y.C.R.; methodology, J.Y.C.R., G.O.S.S., A.R.D. and I.R.; catalytic activity investigation, J.L. and M.A.R.; catalytic activity analysis and interpretation, J.Y.C.R., J.L. and M.A.R.; XRD investigation and data analysis, J.Y.C.R., G.O.S.S., and A.R.D.; TEM investigation and interpretation, J.Y.C.R., G.O.S.S. and A.R.D.; writing—original draft preparation, J.Y.C.R.; writing—review and editing, K.I.B.E., G.R.S.-B. and M.R.V.L.; funding acquisition, J.L. and M.A.R. All authors have read and agreed to the published version of the manuscript.

Funding: This research was funded by the research project TED2021-131630B-I00 granted by MCIN/AEI/10.13039/501100011033/ and "Unión Europea NextGenerationEU/PRTR" and the project SPBLY/21/180501/000075 granted by the JCCM and EU (FEDER). The research was also funded by the Brazilian National Counsel of Technological and Scientific Development, CNPq (grants: 305287/2022-2, 401158/2022-5, and 307866/2022-0), the Coordination for the Improvement of Higher Education Personnel, CAPES (grant: 001), the Sergipe State Research and Technological Innovation Foundation (FAPITEC), and São Paulo Research Foundation (FAPESP, grants #2017/10118-0, #2020/02743-4, #2022/03386-6 and #2022/12818-7).

Data Availability Statement: The data presented in this study are available on request from the corresponding author. The data will be available on request.

Conflicts of Interest: The authors declare no conflicts of interest.

References

1. Gielen, D.; Boshell, F.; Saygin, D.; Bazilian, M.D.; Wagner, N.; Gorini, R. The role of renewable energy in the global energy transformation. *Energy Strategy Rev.* **2019**, *24*, 38–50. [CrossRef]
2. Dagoumas, A.S.; Koltsaklis, N.E. Review of models for integrating renewable energy in the generation expansion planning. *Appl. Energy* **2019**, *242*, 1573–1587. [CrossRef]
3. Wu, J.; Strezov, V. Green technologies and sustainability: A new trend. *Green Technol. Sustain.* **2023**, *1*, 100008. [CrossRef]
4. Sazali, N. Emerging technologies by hydrogen: A review. *Int. J. Hydrogen Energy* **2020**, *45*, 18753–18771. [CrossRef]
5. Megía, P.J.; Vizcaíno, A.J.; Calles, J.A.; Carrero, A. Hydrogen production technologies: From fossil fuels toward renewable sources. A mini review. *Energy Fuels* **2021**, *35*, 16403–16415. [CrossRef]
6. Amrouche, S.O.; Rekioua, D.; Rekioua, T.; Bacha, S. Overview of energy storage in renewable energy systems. *Int. J. Hydrogen Energy* **2016**, *41*, 20914–20927. [CrossRef]
7. Arsad, A.Z.; Hannan, M.A.; Al-Shetwi, A.Q.; Mansur, M.; Muttaqi, K.M.; Dong, Z.Y.; Blaabjerg, F. Hydrogen energy storage integrated hybrid renewable energy systems: A review analysis for future research directions. *Int. J. Hydrogen Energy* **2022**, *47*, 17285–17312. [CrossRef]
8. Lei, J.; Liu, X.; Chen, X.; Guan, P.; Feng, W.; Zhang, J.; Luo, H.; Liu, F.; Zhang, Y. Multi-length-scale heterogeneous structured ion exchange membranes for cost-effective electrolysis and hydrogen production. *Chem. Eng. J.* **2022**, *431*, 133994. [CrossRef]
9. Millet, P. Chlor-alkali technology: Fundamentals, processes and materials for diaphragms and membranes. In *Handbook of Membrane Reactors*; Elsevier: Amsterdam, The Netherlands, 2013; pp. 384–415.
10. Erden, M.; Karakilcik, M. Experimental investigation of hydrogen production performance of various salts with a chlor-alkali method. *Int. J. Hydrogen Energy* **2024**, *52*, 546–560. [CrossRef]
11. Pratter, S.M.; Light, K.M.; Solomon, E.I.; Straganz, G.D. The Role of Chloride in the Mechanism of O_2 Activation at the Mononuclear Nonheme Fe(II) Center of the Halogenase HctB. *J. Am. Chem. Soc.* **2014**, *136*, 9385–9395. [CrossRef]
12. Mirseyed, S.F.; Jafarzadeh, K.; Rostamian, A.; Abbasi, H.M.; Ostadhassan, M. A new insight on the mechanisms of corrosion deactivation of a typical Ti/IrO_2 + RuO_2 +TiO_2 coating in the presence of Ta_2O_5 in chlor-alkali medium. *Corros. Sci.* **2023**, *214*, 111005. [CrossRef]
13. Burke, L.D.; O'Neill, J.F. Some aspects of the chlorine evolution reaction at ruthenium dioxide anodes. *J. Electroanal. Chem. Interfacial Electrochem.* **1979**, *101*, 341–349. [CrossRef]
14. Ferro, S.; De Battisti, A. Electrocatalysis and Chlorine Evolution Reaction at Ruthenium Dioxide Deposited on Conductive Diamond. *J. Phys. Chem. B* **2002**, *106*, 2249–2254. [CrossRef]
15. Carvela, M.; Santos, G.d.O.S.; Gonzaga, I.; Eguiluz, K.; Lobato, J.; Salazar-Banda, G.; Rodrigo, M.A. Platinum: A key element in electrode composition for reversible chloralkaline electrochemical cells. *Int. J. Hydrogen Energy* **2021**, *46*, 32602–32611. [CrossRef]
16. Carvela, M.; Lobato, J.; Rodrigo, M.A. Improving stability of chloralkaline high-temperature PBI-PEMFCs. *J. Electroanal. Chem.* **2021**, *904*, 115940. [CrossRef]

17. Santos, M.O.; de OS Santos, G.; Mattedi, S.; Griza, S.; Eguiluz, K.I.; Salazar-Banda, G.R. Influence of the calcination temperature and ionic liquid used during synthesis procedure on the physical and electrochemical properties of Ti/$(RuO_2)_{0.8}$–$(Sb_2O_4)_{0.2}$ anodes. *J. Electroanal. Chem.* **2018**, *829*, 116–128. [CrossRef]
18. Li, X.; Yan, J.; Zhu, K. Fabrication and characterization of Pt doped Ti/Sb-SnO_2 electrode and its efficient electro-catalytic activity toward phenol. *Eng. Sci.* **2021**, *15*, 38–46. [CrossRef]
19. Zhang, Q.; Liu, Y.; Zeng, D.; Lin, J.; Liu, W. The effect of Ce doped in Ti/SnO_2-Sb_2O_3/SnO_2-Sb_2O_3-CeO_2 electrode and its electro-catalytic performance in caprolactam wastewater. *Water Sci. Technol.* **2011**, *64*, 2023–2028. [CrossRef]
20. Lyons, M.E.; Floquet, S. Mechanism of oxygen reactions at porous oxide electrodes. Part 2—Oxygen evolution at RuO_2, IrO_2 and $Ir_xRu_{1-x}O_2$ electrodes in aqueous acid and alkaline solution. *Phys. Chem. Chem. Phys.* **2011**, *13*, 5314–5335. [CrossRef]
21. Deng, Z.; Xu, S.; Liu, C.; Zhang, X.; Li, M.; Zhao, Z. Stability of dimensionally stable anode for chlorine evolution reaction. *Nano Res.* **2023**, 1–11. [CrossRef]
22. Abe, T.; Inoue, S.; Watanabe, K. XRD and electrochemical measurements of RuO_2 powder treated by using a mechanical grinding method. *J. Alloys Compd.* **2003**, *358*, 177–181. [CrossRef]
23. Sun, Q.; Ren, Q.-Q.; Li, H.; Fu, Z.-W. High capacity Sb_2O_4 thin film electrodes for rechargeable sodium battery. *Electrochem. Commun.* **2011**, *13*, 1462–1464. [CrossRef]
24. Antolini, E.; Cardellini, F. Formation of carbon supported PtRu alloys: An XRD analysis. *J. Alloys Compd.* **2001**, *315*, 118–122. [CrossRef]
25. Cattaneo, C.; de Pinto, M.I.; Sanchez, M.H.; de Mishima, B.A.; López, L.D.; Cornaglia, L. Characterization of platinum-rutheniun electrodeposits using XRD, AES and XPS analysis. *J. Electroanal. Chem.* **1999**, *461*, 32–39. [CrossRef]
26. Duan, T.; Chen, Y.; Wen, Q.; Duan, Y. Different mechanisms and electrocatalytic activities of Ce ion or CeO_2 modified Ti/Sb–SnO_2 electrodes fabricated by one-step pulse electro-codeposition. *Rsc Adv.* **2015**, *5*, 19601–19612. [CrossRef]
27. Chalupczok, S.; Kurzweil, P.; Hartmann, H.; Schell, C. The redox chemistry of ruthenium dioxide: A cyclic voltammetry study—Review and revision. *Int. J. Electrochem.* **2018**, *2018*, 1273768. [CrossRef]
28. Macounová, K.M.; Simic, N.; Ahlberg, E.; Krtil, P. Hypochlorite Oxidation on RuO_2-Based Electrodes: A Combined Electrochemical and In Situ Mass Spectroscopic Study. *Electrocatalysis* **2019**, *10*, 45–55. [CrossRef]
29. Seymour, I.; O'Sullivan, B.; Lovera, P.; Rohan, J.F.; O'Riordan, A. Electrochemical detection of free-chlorine in Water samples facilitated by in-situ pH control using interdigitated microelectrodes. *Sens. Actuators B Chem.* **2020**, *325*, 128774. [CrossRef]
30. Fukuzaki, S. Mechanisms of actions of sodium hypochlorite in cleaning and disinfection processes. *Biocontrol Sci.* **2006**, *11*, 147–157. [CrossRef] [PubMed]
31. Li, K.; Fan, Q.; Chuai, H.; Liu, H.; Zhang, S.; Ma, X. Revisiting chlor-alkali electrolyzers: From materials to devices. *Trans. Tianjin Univ.* **2021**, *27*, 202–216. [CrossRef]
32. Huskinson, B.; Rugolo, J.; Mondal, S.K.; Aziz, M.J. A high power density, high efficiency hydrogen–chlorine regenerative fuel cell with a low precious metal content catalyst. *Energy Environ. Sci.* **2012**, *5*, 8690–8698. [CrossRef]
33. Thomassen, M.; Sandnes, E.; Børresen, B.; Tunold, R. Evaluation of concepts for hydrogen–chlorine fuel cells. *J. Appl. Electrochem.* **2006**, *36*, 813–819. [CrossRef]
34. Jalalpoor, D.; Göhl, D.; Paciok, P.; Heggen, M.; Knossalla, J.; Radev, I.; Peinecke, V.; Weidenthaler, C.; Mayrhofer, K.J.; Ledendecker, M. The Impact of Antimony on the Performance of Antimony Doped Tin Oxide Supported Platinum for the Oxygen Reduction Reaction. *J. Electrochem. Soc.* **2021**, *168*, 024502. [CrossRef]
35. da Silva, L.M.; Santos, G.d.O.S.; de Salles Pupo, M.M.; Eguiluz, K.I.B.; Salazar-Banda, G.R. Influence of heating rate on the physical and electrochemical properties of mixed metal oxides anodes synthesized by thermal decomposition method applying an ionic liquid. *J. Electroanal. Chem.* **2018**, *813*, 127–133. [CrossRef]
36. Da Silva, L.M.; De Faria, L.A.; Boodts, J.F.C. Determination of the morphology factor of oxide layers. *Electrochim. Acta* **2001**, *47*, 395–403. [CrossRef]
37. Carvela, M.; Lobato, J.; Rodrigo, M.A. Storage of energy using a gas-liquid H_2/Cl_2 fuel cell: A first approach to electrochemically-assisted absorbers. *Chemosphere* **2020**, *254*, 126795. [CrossRef]